A New Modulation–Demodulation Approach to DC Power-line Data Transmission for SRG-Integrated Microgrid

Dongsheng Yu, *Member, IEEE*, Yingchun Hua, Shenglong Yu, *Member, IEEE*, Pinjia Zhang, *Senior Member, IEEE*, Herbert H. C. Iu, *Senior Member, IEEE*, and Tyrone Fernando, *Senior Member, IEEE*

***Abstract*—Switched reluctance generators (SRGs) possess a range of advantages, such as simple structure, good heat dissipation, high fault tolerance, which have, thus, been applied to wind power generation systems and other distributed generators. In order to maximize SRG performances, stable and reliable communication is essential to facilitate system monitoring, fault detection, and energy management system development. In this article, we propose a new modulation–demodulation strategy to realize effective power-line communication (PLC) between SRG and other converters in an inverter-interfaced distributed power grid. The newly designed modulation method utilizes and controls the turn-ON/OFF angle (TOA) of an SRG, so as to modulate the voltage ripples to convey information to the receiving end. An innovated demodulation method is also devised in this article, using maximum entropy spectrum estimation (MESE) method, for the purpose of acquiring useful signals from the sending end. Vigorous experimentation is conducted, which verify the functionality of the proposed TOA-MESE modulation–demodulation method for data transmission between SRG and other converter-based installations.**

***Index Terms*—Maximum entropy spectrum estimation (MESE), power and data composite modulation, power-line data transmission, switched reluctance generator (SRG).**

I. Introduction

SWITCHED reluctance generators (SRGs) have been deemed as a promising electricity generation apparatus to be deployed in modern renewable-energy-integrated distributed power grids, due to its wide-ranging advantages such as structural simplicity, good heat dissipation, and high fault tolerance [1]–[3]. For effective control and intelligent power supply, communication is required between SRGs and other converter-based generators or loads in the power grid. Generally speaking, data transmission is realized through wired and wireless channels [4], [5].

Conventionally, data are transmitted via dedicated communication channels, independently from the power transmission lines, such as optical fiber and wireless networks [6], [7]. For optical fiber communication, useful data can be transmitted via independent cables with high reliability, anti-interference ability and very low attenuation. However, the installation and maintenance costs are inevitably high due to the strict requirement of modulation devices and transmission cables. With wireless communication, data can be transmitted without needing physical connection and, hence, has the advantages of simple implementation, high adaptation, and good scalability. However, wireless communication is subjected to signal interference and shielding due to the use of open frequency band [8]. Also, wireless data transmission distance is evidently restricted due to possible signal attenuation in the air.

Power-line communication (PLC) was first proposed in [9] to achieve synchronous power and data transmission through ac power lines [9]. Since data can be transmitted by the physical power line without needing any extra communication lines, PLC has a low cost, high reliability, nd easy installation and, thus, has been used in many industrial applications [10], [11].

In recent years, PLC technology has been extended from ac to dc power networks [11], [12]. In [11], an intelligent PV monitoring scheme was proposed by utilizing the dc bus as the communication channel, where the monitoring data are modulated into high-frequency voltage ripples and transmitted together with electricity. However, a parallel resonant coupling circuit is required for injecting the data into the power line. It has been pointed out that, by using the active switches inside the dc power converters, data can be timely modulated and transmitted through the power line without requiring extra modulation or data injection devices. In [13], the authors proposed two methods, frequency shift keying and phase shift keying, to realize power and signal composite modulation and synchronous transmission. In [14], in order to improve the operation reliability

Manuscript received July 16, 2019; revised November 10, 2019 and February 25, 2020; accepted March 27, 2020. Date of publication April 2, 2020; date of current version July 20, 2020. This work was supported in part by the National Natural Science Foundation of China under Grants 51977208 and 51822705. Recommended for publication by Associate Editor G. De Donato. *(Corresponding authors: Pinjia Zhang, Dongsheng Yu.)*

Dongsheng Yu and Yingchun Hua are with the School of Electrical and Power Engineering, China University of Mining and Technology, Xuzhou 221116, China (e-mail: donsiee@163.com; 18362824684@163.com).

Shenglong Yu is with the School of Engineering, Deakin University, Melbourne, VIC 3216, Australia (e-mail: s.yu@ieee.org).

Pinjia Zhang is with the Department of Electrical Engineering, Tsinghua University, Beijing 100084, China (e-mail: pinjia.zhang@ieee.org).

Herbert H. C. Iu and Tyrone Fernando are with the School of Electrical, Electronic and Computer Engineering, the University of Western Australia, Crawley, WA 6009, Australia (e-mail: herbert.iu@uwa.edu.au; tyrone.fernando@uwa.edu.au).

Color versions of one or more of the figures in this article are available online at http://ieeexplore.ieee.org.

Digital Object Identifier 10.1109/TPEL.2020.2984911

of dc microgrids, a power and data synchronous transmission (PDST) strategy was proposed by modulating the switching frequency of the dc converter to inject data into specific voltage ripples. Using the proposed communication strategy, all microgrid components can share the power flow information transmitted on the same dc bus. A new pulsewidth modulation (PWM) strategy using direct sequence spread spectrum was presented in [15], which is able to reduce output voltage harmonics and realize PLC. The proposed signal modulation and demodulation strategies were experimentally implemented in both Buck and Boost converters. An improved power and signal composite modulation method by using a phase-shift full-bridge converter was designed in [16], without extra communication infrastructure and signal injection devices.

Nevertheless, up to now, there has been no documented work that attempts to apply PDST to SRG-incorporated distributed generation systems. It can be postulated that the introduction of a PDST communication method will enable the SRG-based microgrid system to bear advantageous features like other converter-based microgrids discussed above. However, the special structure and working principle of SRG require innovative designs of PLC methodologies.

In this article, to achieve SRG PLC, a new set of modulation and demodulation approach is proposed, where modulation is achieved by regulating the turn-ON/OFF angles (TOA) of the SRG, which injects the desired signal into the voltage ripple, whereas the demodulation is realized by innovatively adopting the maximum entropy spectrum estimation (MESE) method. We brand this strategy as the TOA-MESE modulation–demodulation method, which is designed for dc power-line data transmission. Experimentations are conducted, which validate the functionality and feasibility of the proposed TOA-MESE-based dc power-line data transmission approach for SGR-integrated distributed grids.

The rest of this article is organized as follows. The SRG-based dc microgrid of Internet is described in Section II. Output voltage ripples of SRG are analyzed in Section III. The proposed modulation and demodulation methods are interpreted in Section IV. Experimentation are conducted and discussed in Section V. Finally, Section VI concludes this article.

II. SRG-Based DC Microgrid

A dc microgrid with a SRG-based wind turbine (WT) power generator is depicted in Fig. 1, where the generated power from SRG-WT is delivered to an energy storage system and dc load via a dc bus. The output voltage of SRG can be stabilized to a known reference voltage by adjusting the duty cycle of the PWM signal applied to the power converters.

Due to the unique double-salient structure, the phase winding inductance of SRG possesses high nonlinearity, making exact modeling impractical. The flux linkage curves in terms of current and rotor position are drawn in Fig. 2 by using the experimentally sampled data of a four-phase 8/6 SRG. It can be seen that the flux linkage of SRG possesses high nonlinearity, which can be enlarged by increasing phase current with the same rotor position. Different from switched reluctance motor, turn-ON

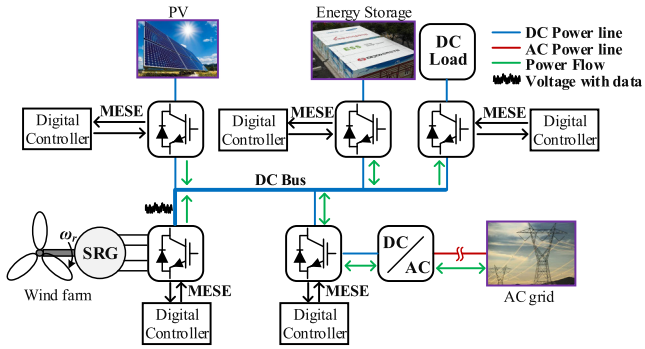

Fig. 1. SRG-based distributed generation system.

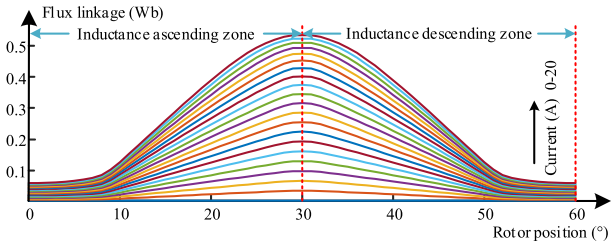

Fig. 2. Flux linkage curves in terms of current and rotor position.

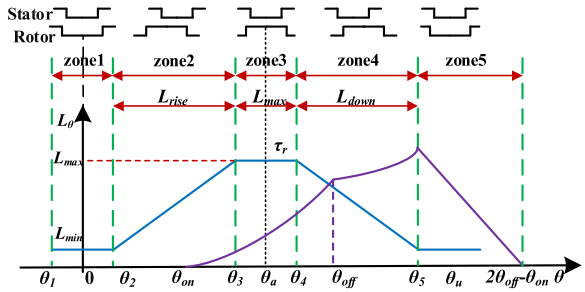

Fig. 3. SRG inductance inside one equivalent operation period.

angle and turn-OFF angles of SRG are restricted in inductance ascending zone and inductance descending zone, respectively, for effectively producing electrical energy. In order to simplify the theoretical calculation, the winding inductance is approximated by linear piecewise function in terms of rotor position, as shown in the following equation, based on which the phase inductance curve inside one period can be drawn, as shown in Fig. 3; this curve can be divided into five regions, i.e., $\theta_1 \rightarrow \theta_2$ (zone 1), $\theta_2 \rightarrow \theta_3$ (zone 2), $\theta_3 \rightarrow \theta_4$ (zone 3), $\theta_4 \rightarrow \theta_5$ (zone 4), and $\theta_5 \rightarrow (2\theta_{\text{off}} - \theta_{\text{on}})$ (zone 5):

$$L(\theta) = \begin{cases} L_{\min} & \theta_1 \le \theta \le \theta_2 \\ L_{\min} + k(\theta - \theta_2) & \theta_2 \le \theta \le \theta_3 \\ L_{\max} & \theta_3 \le \theta \le \theta_4 \\ L_{\max} - k(\theta - \theta_4) & \theta_4 \le \theta \le \theta_5 \end{cases} \tag{1}$$

where $k = (L_{\max} - L_{\min})/(\theta_3 - \theta_2)$.

In zone 1 and zone 5, the poles of stator and rotor are not overlapped and the inductance is at the minimum value $L_{\min}$. In

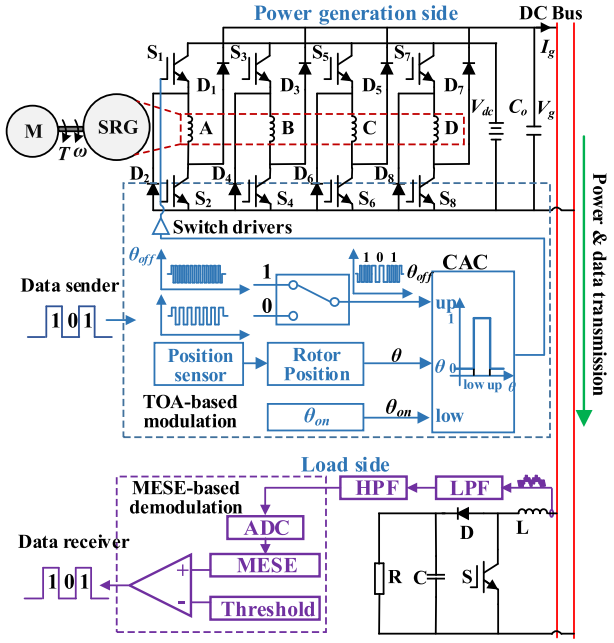

Fig. 4. SRG system with proposed modulation-demodulation strategy.

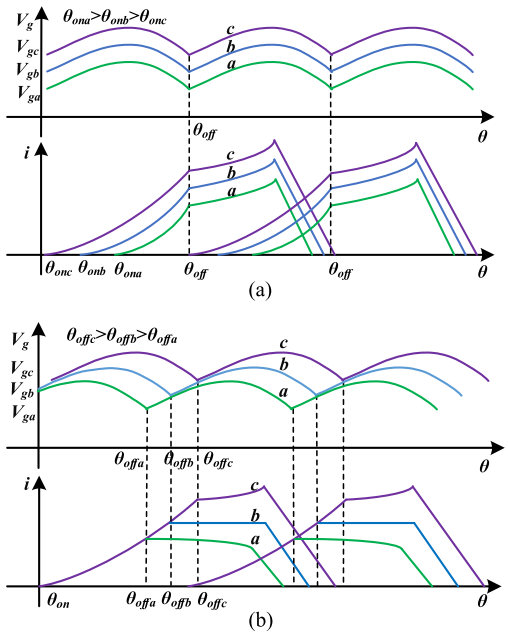

Fig. 5. Output voltage and current in terms of turn-ON and turn-OFF angles. (a) Different turn-ON angles. (b) Different turn-OFF angles.

zone 2, the inductance increases due to the increment of overlapping area of stator and rotor poles. In zone 3, the inductance reaches its maximum value $L_{\max}$ due to the complete overlap between the rotor and stator poles. In zone 4, the inductance decreases as the overlapping area of stator and rotor poles reduces. In addition to rotor position, the phase inductance is also decided by the excitation current. The purple line in Fig. 2 shows the phase current of SRG in terms of rotor positions during power generation. This curve emerges at a turn-ON angle $\theta_{\rm on}$ and completes at position of $2\theta_{\rm off} - \theta_{\rm on}$.

In this article, a four-phase 8/6 SRG connected to a boost converter is employed to incorporate the proposed PLC method. The power converter of SRG is built by an asymmetric half-bridge (AHB) structure circuit, the most widely adopted power converter for the SRG system [17], [18], which is shown in Fig. 4.

To facilitate the implementation of the proposed PLC method, an external excitation mechanism, instead of self-excitation scheme, is chosen in this article for SRG, as external excitation ensures that the excitation voltage and SRG output voltage are independent from each other, which simplifies control design.

As shown in Fig. 4, output voltage and power of SRG can be regulated by tuning the control signals applied to the eight switches of an AHB converter. Also, the source data are modulated using the proposed TOA-based modulation method and implanted into voltage ripples by simultaneously regulating the control signals applied to the two switches of each bridge arm (e.g., S_1 and S_2). The sampled rotor position is inputted into the conduction angle calculator (CAC) to generate the required control signals. The output voltage level of the CAC is high as the rotor position θ satisfies the condition of $\theta_{\rm on} < \theta < \theta_{\rm off}$; otherwise, the zero voltage level is accordingly produced to turn OFF the switches. Sampled and filtered voltage ripples containing the data are then transmitted via the dc bus to the load boost converter, where low-pass and high-pass filters are employed to eliminate the noises. Voltage ripples are demodulated using the proposed MESE-based demodulation method to acquire useful information.

III. Analysis of SRG Output Voltage Ripples

As stated in Section II, voltage ripples are utilized to carry the modulated data. Hence, it is of great importance to investigate the output voltage ripples of the SRG converter.

A. Power Modulation Strategy of SRG

In order to achieve the required output performance of SRG, it is necessary to modulate the control signals applied to converter switches. There are three widely used modulation methods, namely, current chopping control and PWM, angle position control (APC). Among all these methods, APC is adopted in this article due to the fact that the APC method allows the output voltage of SRG to be regulated by the TOA of the two switches of each bridge arm (e.g., S_1 and S_2), which is suitable for the purpose of this article. Detailed comparisons of these modulation methods are documented in [19].

With constant external excitation voltage, the switches of each bridge are only turned ON and OFF once within a commutation period when no data are transmitted, and the waveform of the phase current is determined by the angles of $\theta_{\rm on}$ and $\theta_{\rm off}$, which are located inside zones 2 and 4 in Fig. 3. As shown in Fig. 5(a), with a given constant $\theta_{\rm off}$, the amplitude of the phase current can be altered by changing $\theta_{\rm on}$; hence, the output voltage V_g could be lessened by the decrement of $\theta_{\rm on}$. Likewise, with a constant $\theta_{\rm on}$, the amplitude of the phase current can be adjusted by altering the value of $\theta_{\rm off}$, as shown in Fig. 5(b). Hence, the

turn-ON angle $\theta_{\rm on}$ and turn-OFF angle $\theta_{\rm off}$ can be employed to regulate the output voltage or power.

B. Output Voltage of SRG

The operation process of SRG during a commutation period includes two stages, namely the excitation stage and freewheeling stage. During the excitation stage, the input mechanical and excitation power are converted to electromagnetic energy stored in the stator windings. During the freewheeling stage, the electromagnetic energy stored in SRG windings is released to the dc bus via the power converter.

At the excitation stage ($\theta_{\rm on} \le \theta \le \theta_{\rm off}$), we have

$$V_{\rm dc} = ir - e = ir + \frac{d\psi}{dt} \tag{2}$$

where r is the resistance of phase winding, $V_{\rm dc}$ is the excitation voltage, i is the phase current, e is the induced electromotive force (EMF), and ψ is the winding flux.

At the freewheeling stage ($\theta_{\rm off} \le \theta \le 2\theta_{\rm off} - \theta_{\rm on}$), it can be obtained that

$$V_{\rm dc} = -ir + e = -ir - \frac{d\psi}{dt}. \tag{3}$$

Combining (2) and (3), we have

$$\pm V_{\rm dc} = ir + e = ir + \frac{d\psi}{dt}. \tag{4}$$

Note that, phase voltage ir is relatively small as compared to $d\psi/dt$ and, hence, can be ignored [20]. Since $\psi = Li$, the abovementioned equation can be rewritten as

$$\pm V_{\rm dc} = L\frac{di}{dt} + i\frac{dL}{d\theta}\omega_r \tag{5}$$

where ω_r is the angular velocity, and the second term on the right-hand side of the equation is the phase winding back-EMF.

In order to avoid unexpected effects of the freewheeling current on the operation in the next commutation period, the turn-ON angle $\theta_{\rm on}$ is located inside zone 2 and the turn-OFF angle $\theta_{\rm off}$ is configured inside zone 4.

Phase current $i(\theta)$ can be calculated as the rotor rotates across different angle intervals, which is discussed below.

1) $\theta_{on} \le \theta \le \theta_3$*:* In this interval, the phase inductance increases with the increment of rotor position θ. Assuming that the initial value of the phase current is $i(\theta_{\rm on}) = 0$, $i(\theta)$ can be expressed as

$$i(\theta) = \frac{V_{\rm dc}}{\omega_r k}\left(1 - \frac{k\,(\theta_{\rm on} - \theta_2) + L_{\rm min}}{k\,(\theta - \theta_2) + L_{\rm min}}\right). \tag{6}$$

Note that, $\theta_{\rm on} \ge \theta_2$ and $\theta \ge \theta_2$, $V_{\rm dc}$, ω_r, and k are positive. Hence, it can be deduced that the phase current can be increased by increasing rotor position θ. Take phase A as an example. In order to simplify the analysis, we assume that phase A ends excitation at the position where phase D finishes freewheeling, and phase B starts excitation at position θ_5 of phase. In the interval of $\theta_{\rm on} \le \theta \le \theta_3$, phase A operates in the excitation stage while phase D remains in the freewheeling stage. The current flowing inside the AHB converter inside this interval is shown in Fig. 6, where red and blue curves correspond to excitation and freewheeling, respectively.

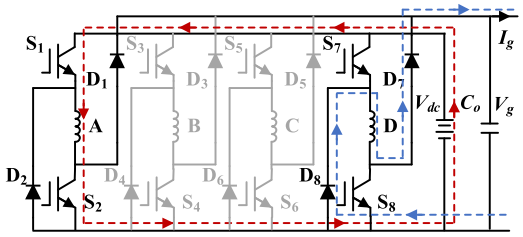

Fig. 6. Current path inside the interval of $\theta_{\rm on} \le \theta \le \theta_3$.

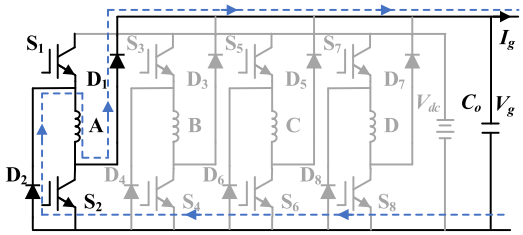

Fig. 7. Current path inside the interval of $\theta_{\rm off} \le \theta \le \theta_5$.

2) $\theta_3 \le \theta \le \theta_4$*:* The phase inductance $L = L_{\rm max}$ during this interval. Based on (5), the phase current can be calculated by

$$i(\theta) = \frac{V_{\rm dc}}{\omega_r L_{\rm max}}(\theta - \theta_{\rm on}). \tag{7}$$

Phase current can be increased at a relatively high rate, and the input mechanical energy and excitation energy are both converted into the magnetic energy stored in the phase windings, and clearly the phase current is linearly proportional to rotor position θ. Phase D finishes freewheeling and phase A operates in the stage of excitation with the same current path, as shown in Fig. 6.

3) $\theta_4 \le \theta \le \theta_{off}$*:* The phase inductance reduces by increasing the angle θ according to $L = L_{\rm max} - k(\theta - \theta_4)$. The phase current $i(\theta)$ can be calculated by

$$i(\theta) = \frac{V_{\rm dc}(\theta - \theta_{\rm on})}{\omega_r[L_{\rm max} - k(\theta - \theta_4)]}. \tag{8}$$

Phases D, B, and C are waiting for activation without current passing through, and phase A still operates in the stage of excitation with the same current path, as shown in Fig. 6.

4) $\theta_{off} \le \theta \le \theta_5$*:* Inside this interval, we have $L = L_{\rm max} - k(\theta - \theta_{\rm off})$, and two switches of phase A are OFF. The phase current flows through the freewheeling diodes to the dc bus. The winding voltage is denoted as V_g and the phase current can be obtained by

$$i(\theta) = \frac{V_g(2\theta_{\rm off} - \theta - \theta_{\rm on})}{\omega_r[L_{\rm max} - k(\theta - \theta_4)]}. \tag{9}$$

The dc bus is powered by phase A and no current passes through phases D, B, and C. The current path inside the AHB converter is shown in Fig. 7.

5) $\theta_5 \le \theta \le 2\theta_{off} - \theta_{on}$*:* Beyond the interval $[\theta_1, \theta_5]$, a narrow region can be found where the freewheeling current is

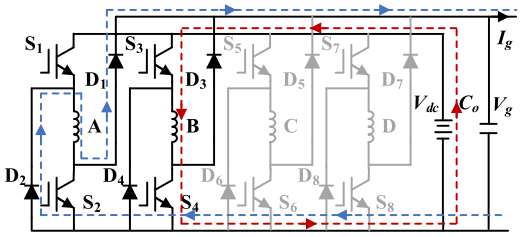

Fig. 8. Current path inside the interval of $\theta_5 \le \theta \le 2\theta_{\rm off} - \theta_{\rm on}$.

nonzero even when the next phase winding starts to be excited. Inside this region, the phase current $i(\theta)$ can be calculated by

$$i(\theta) = \frac{V_g(2\theta_{\rm off} - \theta - \theta_{\rm on})}{\omega_r L_{\min}}. \tag{10}$$

The abovementioned equation reflects that the phase current can be gradually reduced until $\theta = 2\theta_{\rm off} - \theta_{\rm on}$. This is the last interval of the operation process of phase A. The excitation of phase B will start in this interval and the current paths inside the AHB converter are shown in Fig. 8.

Equations (6)–(10) demonstrate five operation stages of one phase in SRG. The first three stages are related to the excitation operation, while the rest two stages, corresponding to (9) and (10), represent the power conversion from the phase winding to the dc bus. The four phases are excited by turns, and one commutation period lasts from $\theta = 0°$ to 60°. The relationship between the output phase current and the rotor position θ for phase A can be expressed as

$$i(\theta_A) = \frac{V_g\left[2\theta_{\rm off} - F\left(\theta_A, \theta_p\right) - \theta_{\rm on}\right]}{\omega_r L\left[F\left(\theta_A, \theta_p\right)\right]} \tag{11}$$

where $\theta_p = 60°$ for the 8/6 four-phase SRG, and $F\left(\theta_A, \theta_p\right)$ is the remainder function, and apparently $\theta_{\rm off} \le F\left(\theta_A, \theta_p\right) \le \theta_p$.

In terms of the last two intervals described by (9) and (10), the current of phase A can be obtained by

$$i(\theta_A) = \begin{cases} \frac{V_g(2\theta_{\rm off} - F(\theta_A,\theta_p) - \theta_{\rm on})}{\omega_r[L_{\max} - k(F(\theta_A,\theta_p) - \theta_4)]} & \theta_{\rm off} \le F\left(\theta_A, \theta_p\right) \le \theta_5 \\ \frac{V_g(2\theta_{\rm off} - F(\theta_A,\theta_p) - \theta_{\rm on})}{\omega_r L_{\min}} & \theta_5 \le F\left(\theta_A, \theta_p\right) \le \theta_p. \end{cases} \tag{12}$$

Assuming that the four phases of SRG are symmetric with identical parameters, and the current of phases B, C, and D can then be expressed as

$$\begin{aligned} i(\theta_B) &= i(\theta_A + \theta_q) \\ i(\theta_C) &= i(\theta_B + \theta_q) \\ i(\theta_D) &= i(\theta_C + \theta_q) \end{aligned} \tag{13}$$

where θ_q is the angular difference between two adjacent phases.

With regards to the 8/6 four-phase SRG, the output current is the summation of the currents of all the active phases. Hence, the current injected to the dc bus can be calculated as

$$I_g = i(\theta_A) + i(\theta_B) + i(\theta_C) + i(\theta_D) \tag{14}$$

where I_g is the output current of the SRG system.

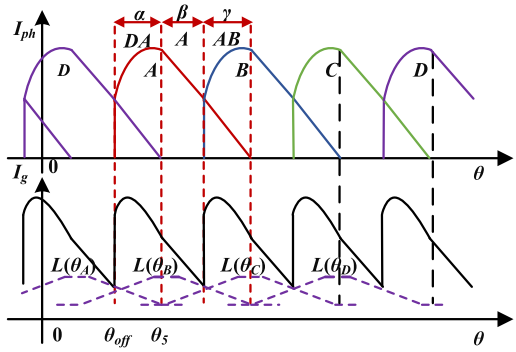

Fig. 9. Output current waveform.

Normally, two adjacent phases of the SRG can be synchronously activated to realize power conversion. The phase current $I_{\rm ph}$ can be divided into three different stages α, β, and γ, as shown in Fig. 9, where the output current I_g is also presented.

For stage α within $\theta_{\rm off}$~θ_5, the output current is in fact the summation of the currents of phases D and A. Symmetrically, the output current of stage γ is the summation of the currents of phases A and B. It can be easily observed that the output current waveforms are periodicity and the period is the summation of two stages α and β. Inside one period, as shown in Fig. 9, the output current I_g can be written as

$$I_g = \begin{cases} i(\theta_A) + i(\theta_D) & \alpha \text{ stage} \\ i(\theta_A) & \beta \text{ stage.} \end{cases} \tag{15}$$

Based on (12), the bus current can be rewritten as

$$I_g = \begin{cases} \frac{V_g\theta_k(L_{\theta_A} - L_{\theta_D} - (\theta_A + \theta_D)(L_{\theta_A} + L_{\theta_D}))}{\omega_r L_{\theta_A} L_{\theta_D}} & \alpha \text{ Stage} \\ \frac{V_g(\theta_k - \theta_A)}{\omega_r L_{\theta_A}} & \beta \text{ Stage} \end{cases} \tag{16}$$

where $\theta_k = 2\theta_{\rm off} - \theta_{\rm on}$, the relation between the output current and output voltage can be described as

$$I_g = C_o \frac{dV_g}{dt} + \frac{P_L}{U_g} \tag{17}$$

where P_L is active power consumption by the load. Assuming the voltage gain of the load converter is *G* and the output voltage is constant, (17) can be rewritten as

$$I_g = C_o \frac{dV_g}{dt} + \frac{G^2 V_g}{R} \tag{18}$$

where *R* is the load resistance. Equation (18) reflects that the output voltage is determined by the output current.

C. Analysis of Output Voltage Ripples

The output voltage ripples can be analyzed from charging and discharging operations of the output capacitor $C_{\rm o}$. By denoting $i_{\rm load}$ as the output current, we have

$$i_{\rm load} = \frac{P_L}{V_g}. \tag{19}$$

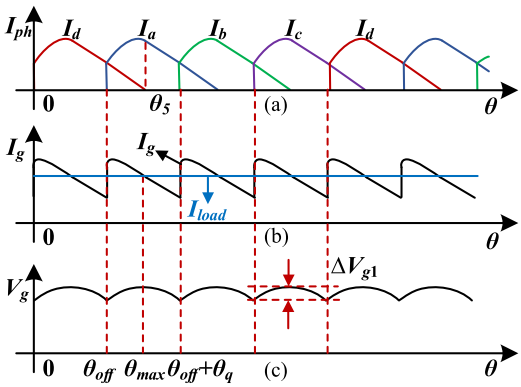

Fig. 10. Ripple analysis of output voltage.

Assuming P_L and V_g remain unchanged, $i_{\rm load}$ can be assumed as a constant for simplifying analysis.

As phase A is operated in the stage of power generation, the output current I_g is greater than the load current $i_{\rm load}$, and the output capacitor $C_{\rm o}$ is being charged, leading to an increasing output voltage V_g. As the rotor position angle θ increases, output current I_g gradually decreases, and $C_{\rm o}$ remains charging until I_g is reduced to $i_{\rm load}$. At the moment of $I_g = i_{\rm load}$, the output voltage V_g can reach its maximum value. When $i(\theta)$ reduces to smaller than $i_{\rm load}$, $C_{\rm o}$ discharges and V_g gradually decreases. V_g will reach its minimum value when activating the next adjacent phase. The phase current, the output current, and the output voltage V_g are shown in Fig. 10.

Note that, the turn-OFF angle $\theta_{\rm off}$ is also the initial position of power generation of phase A. In addition, $\theta_{\rm max}$ shows the position corresponding to $I_g = i_{\rm load}$ and the maximum value of V_g. Therefore, the amplitude of output voltage ripple ΔV_g can be calculated based on the voltage values corresponding to $\theta_{\rm off}$ and $\theta_{\rm max}$.

Load current $i_{\rm load}$ can be approximately calculated based on (16) when $I_g = i_{\rm load}$, which is calculated as follows:

$$i_{\rm load} = I_g = \begin{cases} \frac{V_g\theta_k(L_{\theta_A}-L_{\theta_D}-(\theta_A+\theta_D)(L_{\theta_A}+L_{\theta_D}))}{\omega_r L_{\theta_A} L_{\theta_D}} & \theta_{\rm max} \le \theta_5 \\ \frac{V_g(\theta_k-\theta_A)}{\omega_r L_{\theta_A}} & \theta_{\rm max} > \theta_5 \end{cases} \tag{20}$$

which can be solved by

$$\theta_{\rm max} = \begin{cases} \frac{\theta_q}{2} - \frac{\frac{i_{\rm load}\omega_r L_{\theta_A} L_{\theta_D}}{V_g\theta_k} - L_{\theta_A} + L_{\theta_D}}{2(L_{\theta_A}+L_{\theta_D})} & \theta_{\rm max} \le \theta_5 \\ \theta_k - \frac{i_{\rm load}\omega_r L_{\theta_A}}{V_g} & \theta_{\rm max} > \theta_5. \end{cases} \tag{21}$$

Given that, the rotational speed ω_r and the rotor position angle θ satisfy the condition $\theta = \omega_r t$, (18) can be written as

$$\frac{dV_g}{d\theta} = \frac{1}{C_o\omega_r}\left(I_g - \frac{G^2 V_g}{R}\right). \tag{22}$$

Since the output voltage reaches the minimum and maximum values at $\theta_{\rm off}$ and $\theta_{\rm max}$, respectively, the output voltage ripple ΔV_g can be expressed as

$$\Delta V_{g1} = \int_{\theta_{\rm max}}^{\theta_{\rm off}+\theta_q} \frac{1}{C_o\omega_r}\left(I_g - \frac{G^2 V_g}{R}\right) d\theta. \tag{23}$$

If $\theta_{\rm max} > \theta_5$, according to (21) and (16), we have $\theta_{\rm max} = \theta_k - (i_{\rm load}\omega_{\rm r} L_{\theta \rm a})$ and $I_g = V_g(\theta_k - \theta)/(\omega_{\rm r} L_{\theta \rm a})$. Hence, (23) can be rewritten as

$$\frac{\Delta V_{g1}}{V_g} = \int_{\theta_{\rm max}}^{\theta_{\rm off}+\theta_q} \frac{1}{C_o\omega_r}\left(\frac{2\theta_{\rm off} - \theta_{\rm on} - \theta}{\omega_r L_\theta} - \frac{G^2}{R}\right) d\theta. \tag{24}$$

It can be observed from (24) that the fluctuation amplitude of V_g can be increased by raising the turn-OFF angle $\theta_{\rm off}$.

TABLE I
DIFFERENT SEQUENCES OF PDST MODULATION (MODULATING $\theta_{\rm off}$)

	θ_{on}	θ_{off}
Phases	All phases	A→B→C→D→A→B→C→D
Sequence 1	θ_m	θ_{off1}→θ_{off2}→θ_{off1}→θ_{off2}→θ_{off1}→θ_{off2}→θ_{off1}→θ_{off2}
Sequence 2	θ_m	θ_{off1}→θ_{off1}→θ_{off2}→θ_{off2}→θ_{off1}→θ_{off1}→θ_{off2}→θ_{off2}
Sequence 3	θ_m	θ_{off1}→θ_{off1}→θ_{off1}→θ_{off2}→θ_{off2}→θ_{off2}→θ_{off1}→θ_{off1}
Sequence 4	θ_m	θ_{off1}→θ_{off1}→θ_{off1}→θ_{off1}→θ_{off2}→θ_{off2}→θ_{off2}→θ_{off2}

IV. PROPOSED MODULATION AND DEMODULATION STRATEGIES

A. TOA-Based Modulation Strategies

As presented in Section III, the output voltage of SRG can theoretically be modulated by altering the turn-ON angle $\theta_{\rm on}$ and the turn-OFF angle $\theta_{\rm off}$. Generally speaking, reducing the turn-ON angle $\theta_{\rm on}$ could cause large current at the beginning of the power generation stage, and increasing the turn-OFF angle $\theta_{\rm off}$ can enlarge the excitation time of SRG system as well as output voltage. Four sequences are presented in Table I for regulating the turn-OFF angle $\theta_{\rm off}$, which can be used to achieve PDST modulation. In sequence 1, for example, the turn-OFF angles of the four phases are alternately changed with the order of $\theta_{\rm off1}$→$\theta_{\rm off2}$→$\theta_{\rm off1}$→$\theta_{\rm off2}$→$\theta_{\rm off1}$, while $\theta_{\rm on}$ is constant and $\theta_{\rm on} = \theta_m$. In sequence 2, the phases of A and B are regulated by $\theta_{\rm off1}$ and the phases of C and D are controlled by the turn-OFF angle $\theta_{\rm off2}$. Hence, the variation order of the turn-OFF angle appears periodically as $\theta_{\rm off1}$→$\theta_{\rm off1}$→$\theta_{\rm off2}$→$\theta_{\rm off2}$→$\theta_{\rm off1}$→$\theta_{\rm off1}$. With regards to sequence 3, every three adjacent phases are periodically controlled by the same turn-OFF angles, $\theta_{\rm off1}$ and $\theta_{\rm off2}$, while the turn-ON angle is unchanged. Similarly, every four adjacent phases are periodically regulated by the same turn-OFF angles, $\theta_{\rm off1}$ and $\theta_{\rm off2}$, as listed in the last row of Table I. By regulating the turn-ON angles with constant turn-OFF angles, another four sequences of the PDST method can be obtained, as listed in Table II. It can be deduced from Tables I and II that the frequency of the voltage ripples related to each modulation sequence is different and higher harmonic frequencies can be obtained in sequence 1 since the turn-OFF or turn-ON angles is periodically altered by every commutation period.

In order to explain the data modulation strategy, sequence 1 and sequence 2 are adopted for realizing PDST. As shown in Fig. 11(a) and (b), sequence 1 is adopted when data "1" are transmitted, and sequence 2 is adopted

TABLE II
DIFFERENT SEQUENCES OF PDST MODULATION (MODULATING $\theta_{\rm on}$)

	θ_{on}	θ_{off}
Phases	A → B → C → D → A → B → C → D	All phases
Sequence 1	θ_{off1}→θ_{off2}→θ_{off1}→θ_{off2}→θ_{off1}→θ_{off2}→θ_{off1}→θ_{off2}	θ_n
Sequence 2	θ_{off1}→θ_{off1}→θ_{off2}→θ_{off2}→θ_{off1}→θ_{off1}→θ_{off2}→θ_{off2}	θ_n
Sequence 3	θ_{off1}→θ_{off1}→θ_{off1}→θ_{off2}→θ_{off2}→θ_{off2}→θ_{off1}→θ_{off1}	θ_n
Sequence 4	θ_{off1}→θ_{off1}→θ_{off1}→θ_{off1}→θ_{off2}→θ_{off2}→θ_{off2}→θ_{off2}	θ_n

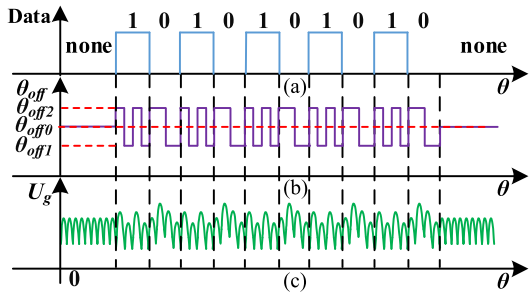

Fig. 11. Output voltage with data transmission.

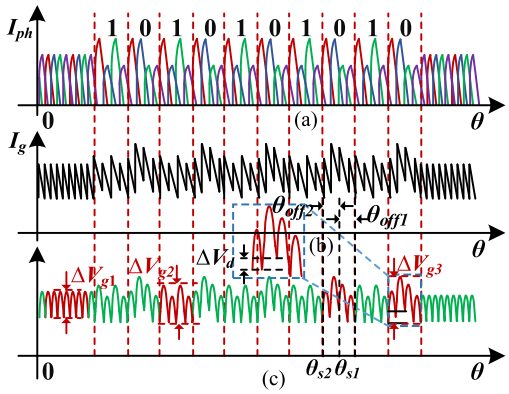

Fig. 12. Ripple analysis of output voltage.

when transmitting data "0." In case of no data transmission, the turn-OFF angle $\theta_{\rm off}$ is configured to $\theta_{\rm off0}$. In order to minimize the impact of signal transmission on the power generation, the turn-OFF angles of $\theta_{\rm off0}$, $\theta_{\rm off1}$, and $\theta_{\rm off2}$ should satisfy the condition of $\theta_{\rm off2} - \theta_{\rm off0} = \theta_{\rm off0} - \theta_{\rm off1}$. The waveforms of the output voltage ripples with data transmission are shown in Fig. 11(c).

The waveforms of phase current, bus current, and output voltage are presented in Fig. 12. The harmonic component of the output voltage ripples can be divided into three parts. The first part is the voltage ripples generated by the commutation operation of SRG, denoted as ΔV_{g1}, shown in Fig. 12(c), and the other two are brought about by the shifting of turn-OFF angles for the data transmission of "1" and "0." As depicted in Fig. 12(c), the voltage ripples related to data "1" and "0" are quite different, which are labeled by ΔV_{g2} and ΔV_{g3}. The voltage ripples with the peak-to-peak value of ΔV_{g2} is brought about by regulating the phase turn-OFF angles with $\theta_{\rm off1}$-$\theta_{\rm off2}$-$\theta_{\rm off1}$-$\theta_{\rm off2}$-$\theta_{\rm off1}$. Generally speaking, $\Delta V_{g2} > \Delta V_{g1}$, which is produced by the turn-OFF angle of $\theta_{\rm off0}$.

According to (23), the peak-to-peak voltage ΔV_{g2} can be calculated by

$$\Delta V_{g2} = \int_{\theta_{\max}}^{\theta_{off2}+\theta_q} \frac{1}{C_o\omega_r}\left(I_g - \frac{G^2V_g}{R}\right)d\theta. \tag{25}$$

The calculation of ΔV_{g3} caused by the transmission of data "0" possesses higher complexity, compared to the calculation of ΔV_{g2}. As shown in Fig. 12(c), the voltage ripples of transmitting data "0" generally bear higher irregularity, and the peak-to-peak value since two adjacent phases are configured by the same turn-OFF angle. It can be deduced that the peak-to-peak value of voltage ripples regulated by sequence 4 is greater than that of sequence 3, sequence 2, and sequence 1, since four adjacent phases are configured with the same turn-OFF angle. In addition, to a considerable extent, the peak-to-peak value of the voltage ripples is also determined by the difference between $\theta_{\rm off2}$ and $\theta_{\rm off1}$, namely, $\theta_{\rm off2} - \theta_{\rm off1} = \Delta\theta_{\rm off}$. The peak-to-peak value of the voltage ripples can be enlarged by increasing $\Delta\theta_{\rm off}$, which needs to be restricted in order to achieve a high power quality.

The voltage ripple of transmitting data "0" is decided by the phase commutation operation and the turn-OFF angle difference. The peak-to-peak value of the voltage ripple caused by the turn-OFF angle operation is denoted by ΔV_d, which is presented in Fig. 12(c). The value of ΔV_{g3} can be approximated by summing ΔV_d and ΔV_{g1}. Assuming θ_{s1} and θ_{s2} are the turn-OFF positions of the phases with turn-OFF angles $\theta_{\rm off1}$ and $\theta_{\rm off2}$, and denoting I_{g1} and I_{g2} as the output bus currents sampled at the positions of θ_{s1} and θ_{s2}, the output voltage ripple ΔV_{g3} can be expressed as

$$\begin{aligned}\Delta V_{g3} &= \Delta V_{g1} + V_g(\theta_{\rm off} = \theta_{\rm off2}) - V_g(\theta_{\rm off} = \theta_{\rm off1}) \\ &= \Delta V_{g1} + \frac{I_{g2}(2\theta_{\rm off2} - \theta_{s2} - \theta_{\rm on})}{\omega_r L(\theta_{s2})} \\ &\quad - \frac{I_{g1}(2\theta_{\rm off1} - \theta_{s1} - \theta_{\rm on})}{\omega_r L(\theta_{s1})}.\end{aligned} \tag{26}$$

In order to simplify the calculation, the inductances at these two positions are approximated to be equal since $\Delta\theta_{\rm off}$ is relatively small, namely, $L(\theta_{s1}) = L(\theta_{s2}) = L$. Also, I_{g1} and I_{g2} are also approximated to be equal and represented as I_g. Therefore, (26) can be written as

$$\Delta V_{g3} = \Delta V_{g1} + \frac{I_g(2\Delta\theta_{\rm off} - \Delta\theta)}{\omega_r L(\theta)} \tag{27}$$

where $\Delta\theta = \theta_{s2} - \theta_{s1}$, which is a constant, and the variation of voltage ripple ΔV_{g3} is decided by $\Delta\theta_{\rm off}$. A larger $\Delta\theta_{\rm off}$ leads to a larger voltage ripple.

B. MESE-Based Demodulation Method

The injected data in the voltage ripples can be demodulated by extracting the harmonic frequency of the sampled bus voltage. However, with regards to traditional FFT, in order to obtain high resolution, high sampling frequency and suitable window function are required, which increases the computational burden within a short sampling time. Compared to FFT, the MESE

method can achieve high estimation accuracy with a limited number of data, especially fast sampled data and signals.

The principle of MESE is to approximate autocorrelated sequences x_{m+1}, $x_{m+2}\ldots$, from the known data sequences $x_1, x_2, \ldots, x_m$ without extra assumptions.The entropy of the data sequence can be calculated by

$$H(x) = E[x_j] = \sum_{j=1}^{m} x_j \lg \frac{1}{x_j}. \tag{28}$$

The term entropy is the average amount of the information sent by the data source according to (28). When the time of this process tends to be infinite, or $m \to \infty$, another measure is adopted as follows:

$$H(s(f)) = \frac{1}{4f_N} \int_{-f_N}^{f_N} \lg(s(f))df \tag{29}$$

where $[-f_N, f_N]$ is the frequency range and $s(f)$ is the power spectrum.

In order to find the maximum value, the Lagrange multiplier method is employed, i.e., the result can be obtained by

$$\frac{\partial}{\partial S(f)} \left\{ \frac{1}{4f_N} \int_{-f_N}^{f_N} \lg(s(f))df + \sum_{m=-p}^{p} \lambda_m (R(m)) - \frac{1}{4f_N} \int_{-f_N}^{f_N} s(f) \exp(j2\pi f k \Delta t) df \right\} = 0 \tag{30}$$

where $R(m)$ is the data sequence, $m = 0, \pm 1, \pm 2, \ldots, \pm p$, and λ_m is the coefficient in the Lagrange multiplier method.

Solving (30) yields

$$\frac{1}{s(f)} = \sum_{m=-p}^{p} \lambda_m \exp(j2\pi f m \Delta t). \tag{31}$$

The right-hand side of (31) can also be rewritten as

$$\sum_{m=-p}^{p} \lambda_m z^m = G(z) G^*\left(\frac{1}{z^*}\right) \tag{32}$$

where $z = \exp(j2\pi f m \Delta t)$, and $G(z) = \sum_{k=\ 0}^{p} b_k z^{-k}$, $k = 0, \pm 1, \pm 2, \ldots, \pm p$. Normalizing $G(z)$, we can have

$$\frac{G(z) G^*\left(\frac{1}{z^k}\right)}{g(0) g^*(0)} = A(z) A\left(\frac{1}{z^*}\right) \tag{33}$$

where $1/(g(0)g^*(0)) = P_M/(2f_N)$, and P_M is output power of an M-order prediction error filter. $g(0)$ is the initial value of inverse transformation of z of $G(z)$, and $A(z)$ is the system function.

Given that $A(z) = 1 + \sum_{k=\ 1}^{p} a_k z^{-k}$, the maximum entropy power spectrum can be written as

$$S(f) = \frac{P_M}{2f_N \left| 1 + \sum_{k=1}^{M} a_k \exp(-j2\pi f k \Delta t) \right|^2}. \tag{34}$$

The MESE-based data demodulation process is shown in Fig. 13. When no data are being transmitted, the output voltage V_g contains only the voltage ripple of phase commutation; when the data "1" is transmitted, extra voltage ripple ΔV_{g2} is injected into the output voltage V_g, and when data "0" is being transmitted, the voltage ripple with the peak-to-peak value of ΔV_{g3} can be detected. The calculated entropy can be divided into two parts, namely Et_1 and Et_2, which can demodulate data "1" and data "0," respectively, as shown in Fig. 13(c). Considering possible sampling errors and signal attenuation during transmission, the MESE values Et_1 and Et_2 are supposed to be identifiable with adequate magnitudes for the demodulation operation. Hence, demodulation threshold X_{th1} is introduced; namely, only voltage ripples with estimation values (Et_1 and Et_2) greater than X_{th1} are deemed to be effective for signal demodulation. Based on the given value of X_{th1}, the minimum required ripple amplitudes for transmitting data "1" and "0" can be obtained by backstepping calculation of (28)–(34). In order to continuously obtain the transmitted data, the difference between Et_1 and Et_2, namely $Et = Et_1 - Et_2$, is taken for demodulating the data, as shown in Fig. 13(d). Then the calculated entropy difference Et is compared with the preset threshold X_{th2}, and an appropriate threshold can be chosen to avoid demodulation failure. When Et is greater than the threshold X_{th2}, data "1" is confirmed; on the other hand, when Et is less than X_{th2}, data "0" is received. As shown in Fig. 13(e), due to the time T_s required for sampling operation and MESE calculation, time delay T_{delay} between the source data and the demodulated data is observed.

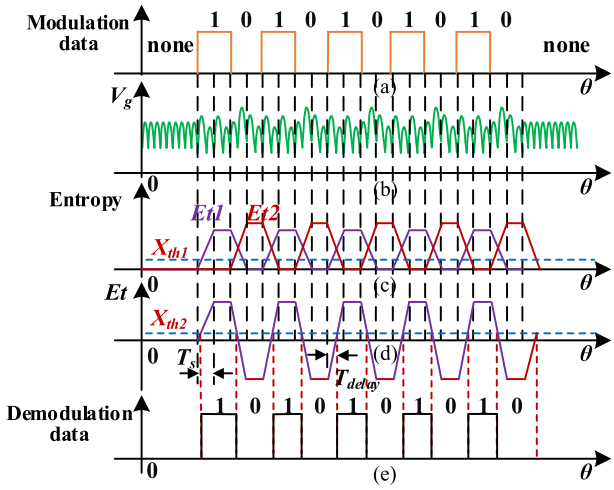

Fig. 13. Demodulation process of output voltage.

It is noteworthy that although the demodulation method can be applied to several of PLC scenarios, the modulation method is specifically designed for the SRG based on its unique operation characteristics. It is a common practice in PLC research and industry to design a dedicated modulation method for a particular type of an inverter-interfaced generator.

V. Experimental Verification and Discussions

A. Experimentation

In order to validate the feasibility of the proposed TOA-MESE-based PDST strategy, experimentation of the SRG system is carried out. Useful parameters of the SRG system are listed in Table III. The experimental platform is built by using

TABLE III
PARAMETERS OF THE SRG SYSTEM

Symbol	Parameter	Value
P	rated power	500 W
p_s	stator pole number	8
p_r	rotor pole number	6
r	phase winding resistance	8Ω
L	phase winding inductance	30mH
V_{dc}	excitation	48 V
n	speed	1200 rpm
V_g	output voltage	48 V
C_o	output capacitor	680 uF
θ_{on}	turn-on angle	20°
θ_{off0}	turn-off angle (no signal)	48°
$\theta_{off1}/\theta_{off2}$	turn-off angle (signal)	47°/49°
f_{s0}	switching frequency of θ_{off} (signal 0)	120 Hz
f_{s1}	switching frequency of θ_{off} (signal 1)	240 Hz
f_c	frequency of the commutation ripple	480 Hz
f_{smp}	DSP sample frequency	12 kHz
T_s	Time window of data sampling	4.2ms

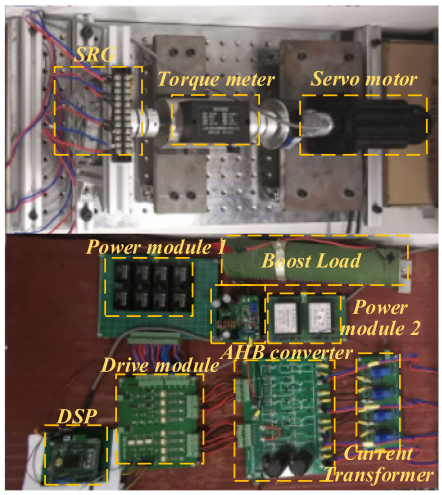

Fig. 14. Experimental setup.

DSP TMS320-F28335, four-phase AHB power converter, SR machine, and a servo motor as an emulator for the WT, as shown in Fig. 14. Microgrids with 48-V dc buses have been investigated and applied for many years [21]–[24]. In this article, the SRG-integrated microgrid configured with 48-V dc buses is adopted for validating the proposed TOA-MESE modulation–demodulation method.

The SRG is driven by the servo motor at a speed of 1200 r/min, and the excitation voltage $V_{\rm dc}$ is 48 V. The upper and lower switching tubes are normally turned ON when the corresponding phase is excited. When no data are sent, the turn-OFF angle $\theta_{\rm off0}$ is configured to 48°; When data "1" and "0" are being transmitted, the turn-OFF angle $\theta_{\rm off}$ is switched between 47° and 49° with the frequency of 240 Hz and 120 Hz, respectively. The frequency of the commutation ripple fc is 480 Hz, which is determined by the speed of 8/6 four-phase SRG. In order to ensure a good performance of demodulation, the A/D sampling frequency $f_{\rm smp}$ is selected to be 12 kHz, and the time width of data sampling T_s for MESE calculation is the four times that of one commutation ripple period.

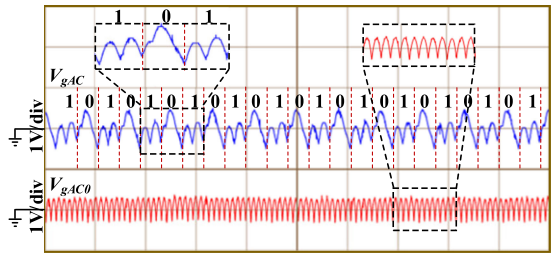

Fig. 15. Sampled voltage and current waveforms of SRG.

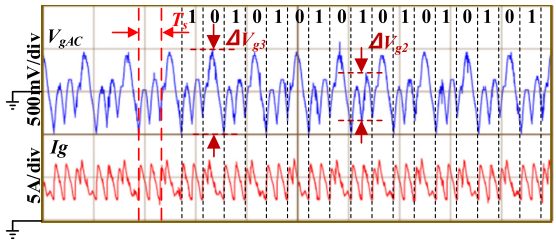

Fig. 16. Output voltage ripples for sending data.

At the receiving end, the voltage ripples on the dc bus are sampled by voltage sensors and converted to low-voltage signals for demodulation. A high-pass filter is employed to remove the dc component of the voltage ripple. The ac component of output voltage V_g with and without data transmission operation ($V_{g\rm AC}$ and V_{gAC0}) of the SRG system is shown in Fig. 15. It can be seen that voltage ripples on dc bus emerge with a constant frequency of 480 Hz and amplitude of 0.34 V as no data are transmitted, and the voltage ripple amplitude increases to 0.47 V by introducing the proposed TOA modulation method. The voltage ripple $V_{g\rm AC}$ and output current $I_{\rm g}$ are shown in Fig. 16 along with the modulated data. It can be also measured that extra voltage harmonics are generated during the data transmission, where the peak-to-peak value of voltage ripple ΔV_{g2} is 0.56 V when data "1" is transmitted, which is 0.479% of the output dc voltage. When data "0" is transmitted, the peak-to-peak value of voltage ripple ΔV_{g3} goes to 0.94 V, 0.979% of the output voltage. However, the influence of ΔV_{g2} and ΔV_{g3} on the overall power generation system is negligible since the signal transmission time is very short, compared to the whole operation process of power generation. In addition, although voltage ripples are required, the communication capability is empowered to the SRG system by the proposed strategy, which is critical for improving the overall operation performance of SRG.

Using the proposed MESE-based demodulation method, entropies Et_1 and Et_2 as well as the entropy difference Et are obtained and shown in Fig. 17. Threshold $X_{\rm th}$ is set to be 0 dB, as shown in the dashed line. The entropy difference Et is used to demodulate data "0" and "1," respectively, as shown in Fig. 17.

The upper and lower waveforms shown in Fig. 18 are the modulated data sent by SRG and the data demodulated by the MESE method, respectively. Data "1" and "0" are alternately sent with 16.7 ms time duration. Time delay $T_{\rm delay}$ between the modulated data and demodulated data can be observed, which is measured to be about 4.2 ms. This demodulation delay $T_{\rm delay}$ is

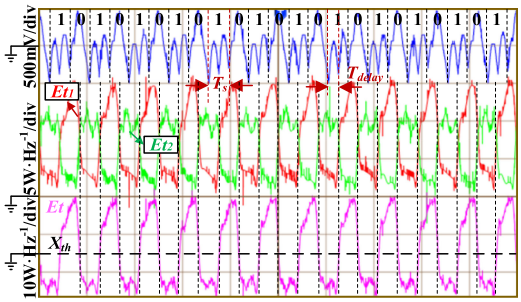

Fig. 17. Demodulation waveforms of output voltage.

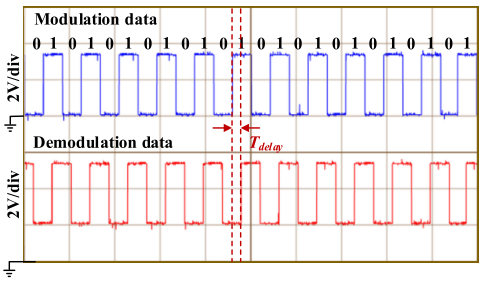

Fig. 18. Waveform of sent data and the received data.

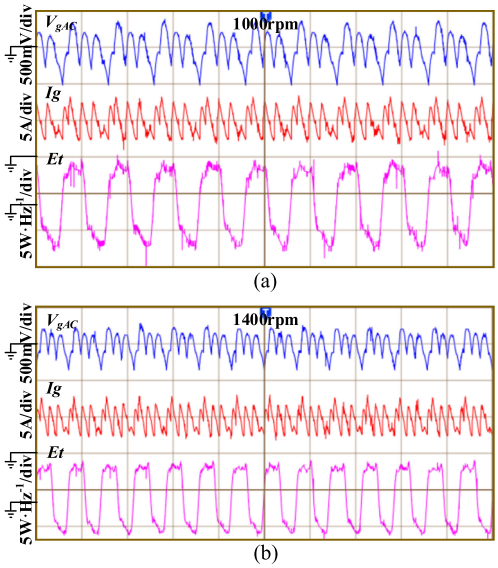

Fig. 19. Experimental waveforms of different driving speeds. (a) 1000 r/min. (b) 1400 r/min.

attributed to the operation of data sampling, MESE calculation, and other processing time required by the DSP. However, it can be observed that the time delay $T_{\rm delay}$ is much smaller than the duration of the useful signal, which guarantees demodulation effectiveness and that there is no mission data.

In order to further validate the proposed TOA-MESE modulation–demodulation method with different wind speeds, the experimental results of 1000 and 1400 r/min rotating speeds are presented in Fig. 19. It can be seen that the entropy difference E_t can be successfully calculated based on the sampled voltage

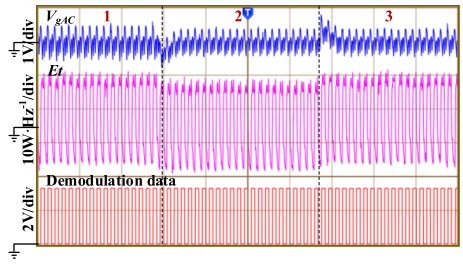

Fig. 20. Demodulation at different load conditions. Interval 1:330 W; Interval 2:560 W; Interval 3: 260 W.

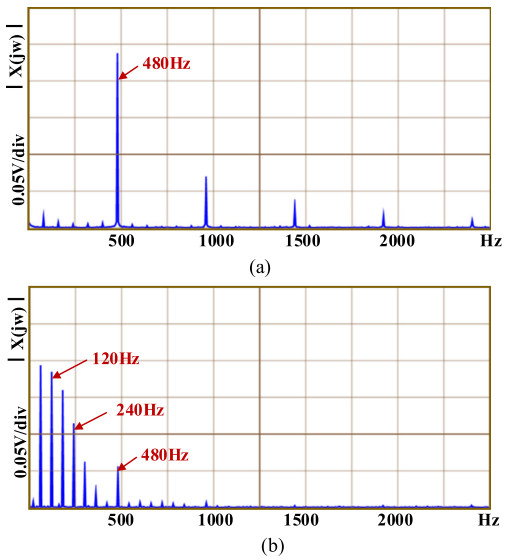

Fig. 21 Amplitudes of output voltage ripples in frequency spectrum. (a) Without data transmission. (b) With data transmission.

ripples, which indicates that the data can be also modulated and demodulated by the proposed TOA-MESE strategy. These sampled voltage ripples also evidently show that the amplitude of voltage ripples for carrying data are reduced by increasing the driving speed of SRG. Hence, the variation value of the turn-OFF angle can be adjusted accordingly to maintain proper amplitude of the voltage ripples to ensure good power quality.

In order to validate the feasibility of the proposed TOA-MESE modulation–demodulation strategy under different load conditions, the load connected to the SRG varies from 330 to 560 W, and then from 560 to 260 W. As shown in Fig. 20, the output voltage can be regulated to its reference via short transient intervals as the output power varies. It can be observed that the voltage ripples corresponding to different output power values are almost the same, and the transmitted data can be timely demodulated even at transient stages of output voltage caused by load variation. This result reveals that the proposed TOA-MESE modulation–demodulation strategy is independent of output power variation.

The frequency spectrum of output voltage ripples with and without data transmission are presented in Fig. 21 for comparison. With regards to the case without TOA modulation, as

TABLE IV
COMPARISON OF PROPOSED STRATEGY WITH EXISTING METHODS

Comparison	Modulation Converters	Modulation Variable	Injection Devices	Demodulation Strategy	Switching Frequency	Data Rate
This method	SRG	Turn-off angle	None	MESE	240Hz	0.2kb/s
[11]	None	Amplitude	Yes	Envelope	200kHz	10kb/s
[13]	Buck or Boost	Frequency	None	DFT	100kHz	2kb/s
[14]	DAB	Frequency	None	FFT	50kHz	5kb/s
[15]	Buck	Phase	None	DFT	400kHz	6.67kb/s
[16]	PSFB	Phase	None	DFT	50kHz	5kb/s

Remarks: MESE—maximum entropy spectrum estimation; PSFB—phase shift full-bridge; DAB—dual active bridge.

shown in Fig. 21(a), it can be measured that the amplitudes of harmonics at 480, 960, 1440, and 1920 Hz are 0.235, 0.072, 0.039, and 0.028 V, respectively, which are induced by inherent phase commutations of the SRG. The frequency spectrum is evidently altered by the proposed TOA modulation, as shown in Fig. 21(b). The harmonics at 60, 120, 180, 240, 300, and 360 Hz can now be observed with amplitudes of 0.193, 0.176, 0.162, 0.117, 0.068, and 0.029 V, respectively, where harmonic ripples of 120 and 240 Hz are purposefully generated for carrying the transmitted data. The harmonic amplitude of 480 Hz induced by phase commutation is attenuated to 0.056 V. This reveals that the maximum amplitude of harmonic ripples with TOA modulation is only 0.402% of the dc bus voltage, and thus, the electromagnetic interference induced by the proposed TOA modulation is small.

In dc microgrid, noises and voltage ripples of different frequencies could be brought about by converters connected to the dc-link. In the proposed PLC strategy, the data are modulated into voltage ripples with a specific frequency. Generally, the voltage ripples generated by SRG possesses a much lower frequency than other power converters. Also, the proposed MESE demodulation strategy is capable to extract signals with any specific frequency. Hence, the proposed PLC strategy can still work even though there are noises and voltage ripples on the dc bus.

When multiple SRGs are connected to the same single dc bus, the proposed PLC strategy can also be employed by appropriately configuring the voltage ripples (signal carrier) modulated by each SRG with a unique frequency. For demonstrative purpose, we only conducted experiments on one SRG connected in a dc microgrid. Multiple SRGs can be realized by repeating the same procedure, yet with a different frequency.

B. Discussions

Referring to the theoretical calculation and the experimental test, it can be summarized that as compared with other PLC strategies used in dc power systems, the proposed strategy has the following advantages.

1) With regards to the traditional PLC strategies, where the signals are modulated by dedicated modulation device, power amplifier and signal injection devices are required for signal transmission on dc bus, such as the strategy discussed in [11]. For the proposed strategy in this article, the signals are compositely modulated together with the electric power by existing power switches without needing extra devices and, hence, could lead to lower cost and volume.
2) The reported power and signal composite modulation strategies are executed on dc/dc converters with relatively high power switching frequencies, as listed in Table IV below (see [11], [13]–[16]), where most of the switching frequencies are greater than 50 kHz. Serious mutual interferences may happen when the signal carriers with similar frequencies are simultaneously transmitted on the same dc bus. The newly proposed modulation strategy for achieving PLC is specifically designed for SRG-integrated dc microgrid. Since the switching frequency of SRG is much lower than dc/dc converters, the low-frequency band of the communication channel can be utilized for transmitting signals (frequency division multiplexing), and hence, the bandwidth efficiency can be increased, which is greatly useful for a microgrid system.
3) An innovated demodulation method is devised by using the MESE method in this article, for the purpose of acquiring useful signals at the receiving end. With regards to traditional FFT, in order to obtain a high resolution, high sampling frequency and suitable window function are required, which increases the computational burden within a short sampling timeframe. Compared to FFT, the MESE method can achieve high estimation accuracy with a limited number of fast-sampled data and signals.

However, there are also two main limitations of the proposed modulation and demodulation strategy, which generally include the following.

1) The proposed modulation strategy can only be used for the SRG converter since the turn-OFF angle is employed for bringing out carrier voltage.
2) In order to guarantee the power quality, the amplitude of voltage ripples produced by power switches for signal modulation is restricted, and hence, the signal transmission distance is also limited.

3) Voltage ripples are indispensable for achieving signal transmission via dc bus, and hence, the proposed strategy cannot be used for microgrid systems requiring ripple-free dc-link configuration.

The comparison of proposed strategy with existing methods is listed in Table IV.

Note that, the transmission performance is greatly affected by the impedance of the transmission line. The communication medium is highly sensitive to high frequencies due to mismatching effects from discontinuities and unmatched loads. A highly frequency-dependent behavior is also shown by the line impedance, i.e., the impedance at the transmitter port or at the receiving port [25].

In fact, the access impedance of the power-line channel is time variant, which is the main cause of impedance mismatch between the access and output impedances of the PLC system, and impedance mismatch will degrade the signal-to-noise power ratio at the communication receiver and, thus, affects transmission distance and reliability [26], [27]. Many strategies have been proposed to resolve the impedance mismatch problem in order to improve the communication-signal transfer from the sending to the receiving side [28]. Due to the complexity of the microgrid system, extensive research effort is required to deal with the impedance mismatch issues. In this article, our research effort only concentrates on the TOA-MESE modulation–demodulation approach to dc power-line data transmission instead of resolving the impedance mismatch problem.

VI. Conclusion

In this article, we have proposed a new dc power-line data transmission strategy with a newly designed TOA-MESE modulation–demodulation method for SRG-based microgrids, which utilizes the advantageous features of APC in SRG to realize TOA-based modulation and also MESE for demodulation. The proposed TOA-MESE method does not require any extra apparatus to achieve PDST in the power grid, posing great economic and constructional benefits with proven feasibility in the experimentation. This strategy also bears high accuracy and low computational burden via using the advanced MESE method for demodulation. The proposed TOA-MESE power-line data transmission method will have wide applicability in emerging SRG-integrated microgrids with renewable energy sources, with a particular practicality for low-speed communication scenarios such as ramping-up and shutting-down generators, resetting, and alarming.

Acknowledgment

Professor Pinjia Zhang is leading the research project "DC Power-line Data Transmission for Microgrid" the authors are working on. He is also responsible for the technical and financial support for the research of this article.

References

[1] A. Takahashi, H. Goto, K. Nakamura, T. Watanabe, and O. Ichinokura, "Characteristics of 8/6 switched reluctance generator excited by suppression resistor converter," *IEEE Trans. Magn.*, vol. 42, no. 10, pp. 3458–3460, Oct. 2006.

[2] D. A. Torrey, "Switched reluctance generators and their control," *IEEE Trans. Ind. Electron.*, vol. 49, no. 1, pp. 3–14, Feb. 2002.

[3] Y. Chang and C. Liaw, "Establishment of a switched-reluctance generator-based common DC microgrid system," *IEEE Trans. Power Electron.*, vol. 26, no. 9, pp. 2512–2527, Sep. 2011.

[4] V. N. Swamy *et al.*, "Real-time cooperative communication for automation over wireless," *IEEE Trans. Wireless Commun.*, vol. 16, no. 11, pp. 7168–7183, Nov. 2017.

[5] V. Srovnal and Z. Machacek, "Industrial communication network for wire and wireless data transfer," in *Proc. Int. Conf. Appl. Electron.*, 2010, pp. 315–318.

[6] C. E. Capovilla, I. R. S. Casella, A. J. S. Filho, T. A. dos Santos Barros, and E. R. Filho, "Performance of a direct power control system using coded wireless OFDM power reference transmissions for switched reluctance aerogenerators in a smart grid scenario," *IEEE Trans. Ind. Electron.*, vol. 62, no. 1, pp. 52–61, Jan. 2015.

[7] Z. Zhao, B. Zhao, and Y. Xia, "Research on the application of optical fiber communication technology in electric power communication," in *Proc. 4th Int. Conf. Model. Simul.*, 2015, pp. 29–32.

[8] H. L. Li *et al.*, "Self-interference cancellation enabling high-throughput short-reach wireless full-duplex communication," *IEEE Trans. Wireless Commun.*, vol. 17, no. 10, pp. 6475–6486, Oct. 2018.

[9] A. Pinomaa, J. Ahola, A. Kosonen, and P. Nuutinen, "Power line communication network for a customer-end AC Grid in an LVDC distribution system," in *Proc. IEEE Int. Conf. Smart Grid Commun.*, 2014, pp. 224–229.

[10] Y. Zhu, J. D. Wu, R. C. Wang, Z. Lin, and X. He, "Embedding power line communication in photovoltaic optimizer by modulating data in power control loop," *IEEE Trans. Ind. Electron.*, vol. 66, no. 5, pp. 3948–3958, May 2019.

[11] W. Mao, X. Zhang, R. Cao, F. Wang, T. Zhao, and L. Xu, "A research on power line communication based on parallel resonant coupling technology in PV module monitoring," *IEEE Trans. Ind. Electron.*, vol. 65, no. 3, pp. 2653–2662, Mar. 2018.

[12] G. Artale *et al.*, "A new low cost coupling system for power line communication on medium voltage smart grids," *IEEE Trans. Smart Grid*, vol. 9, no. 4, pp. 3321–3329, Jul. 2018.

[13] J. Wu, J. Du, Z. Lin, Y. Hu, C. Zhao, and X. He, "Power conversion and signal transmission integration method based on dual modulation of DC–DC converters," *IEEE Trans. Ind. Electron.*, vol. 62, no. 2, pp. 1291–1300, Feb. 2015.

[14] H. Choi and J. Jung, "Enhanced power line communication strategy for DC microgrids using switching frequency modulation of power converters," *IEEE Trans. Power Electron.*, vol. 32, no. 6, pp. 4140–4144, Jun. 2017.

[15] R. Wang, Z. Lin, J. Du, J. Wu, and X. He, "Direct sequence spread spectrum-based PWM strategy for harmonic reduction and communication," *IEEE Trans. Power Electron.*, vol. 32, no. 6, pp. 4455–4465, Jun. 2017.

[16] J. Du, J. Wu, R. Wang, Z. Lin, and X. He, "DC power-line communication based on power/signal dual modulation in phase shift full-bridge converters," *IEEE Trans. Power Electron.*, vol. 32, no. 1, pp. 693–702, Jan. 2017.

[17] J. K. Han, J. W. Kim, and G. W. Moon, "A high-efficiency asymmetrical half-bridge converter with integrated boost converter in secondary rectifier," *IEEE Trans. Power Electron.*, vol. 32, no. 11, pp. 8237–8242, Nov. 2017.

[18] C. O. Yeon, J. B. Lee, I. O. Lee, and G.-W. Moon, "Wide ZVS range asymmetric half-bridge converter with clamp switch and diode for high conversion efficiency," *IEEE Trans. Ind. Electron.*, vol. 63, no. 5, pp. 2862–2870, May 2016.

[19] H. Chen and Q. Wang, "Modeling of switched reluctance linear launcher," *IEEE Trans. Plasma Sci.*, vol. 41, no. 5, pp. 1123–1130, May 2013.

[20] C. Zhang, K. Wang, S. Zhang, X. Zhu, and L. Quan, "Analysis of variable voltage gain power converter for switched reluctance motor," *IEEE Trans. Appl. Supercond.*, vol. 26, no. 7, Oct. 2016, Art. no. 0610905.

[21] D. Boroyevich, I. Cvetković, D. Dong, R. Burgos, F. Wang, and F. Lee, "Future electronic power distribution systems a contemplative view," in *Proc. 12th Int. Conf. Optim. Elect. Electron. Equip.*, May 2010, pp. 1369–1380.

[22] D. Salomonsson and A. Sannino, "Low-voltage DC distribution system for commercial power systems with sensitive electronic loads," *IEEE Trans. Power Del.*, vol. 22, no. 3, pp. 1620–1627, Jul. 2007.

[23] W. Schulz, "ETSI standards and guides for efficient powering of telecommunication and datacom," in *Proc. 29th Int. Telecommun. Energy Conf.*, Rome, Italy, Oct. 2007, pp. 168–173.

[24] Y. Liu, A. Pratt, P. Kumar, M. Xu, and F. C. Lee, "390V input VRM for high efficiency server power architecture," in *Proc. 22nd Annu. IEEE Appl. Power Electron. Conf. Expo.*, Anaheim, CA, USA, Mar. 2007, pp. 1619–1624.
[25] H. C. Ferreira, L. Lampe, J. Newbury, and T. G. Swart, *Power Line Communications: Theory and Applications for Narrowband and Broadband Communications Over Power Lines*. Hoboken, NJ, USA: Wiley, 2010.
[26] M. D. Piante and A. M. Tonello, "On impedance matching in a power-line-communication system," *IEEE Trans. Circuits Syst. II, Express Briefs*, vol. 63, no. 7, pp. 653–657, Jul. 2016.
[27] N. Taherinejad, L. Lampe, and S. Mirabbasi, "An adaptive impedance-matching system for vehicular power line communication," *IEEE Trans. Veh. Technol.*, vol. 66, no. 2, pp. 927–940, Feb. 2017.
[28] A. Petrus, J. V. Rensburg, and H. C. Ferreira, "Design of a bidirectional impedance-adapting transformer coupling circuit for low-voltage power-line communications," *IEEE Trans. Power Del.*, vol. 20, no. 1, pp. 64–70, Jan 2005.

Dongsheng Yu (Member, IEEE) received the B.Eng. and Ph.D. degrees from the School of Information and Electrical Engineering, China University of Mining and Technology, Xuzhou, China, in 2005 and 2011, respectively.

From 2009 to 2010, he was a Visiting Student with The University of Western Australia, Australia, where he became an Endeavour Research Fellow. He is currently a Full Professor with the School of Electrical and Power Engineering, China University of Mining and Technology. His research interests include power electronics, power line communication, fault monitoring and diagnosis, nonlinear dynamics, and memristive systems. He has authored and coauthored two books and more than 60 papers in these areas.

Yingchun Hua received the B.S. degree in water resources and energy power engineering from Yangzhou University, Yangzhou, China, in 2018. He is currently working toward the master's degree with the School of Electrical and Power Engineering, China University of Mining and Technology.

His research interests include switched reluctance generators, power/signal synchronous transmission, dc microgrids.

Shenglong Yu (Member, IEEE) received the master's degree in electrical and electronic engineering and the Ph.D. degree in electrical power engineering from The University of Western Australia (UWA), Perth, WA, Australia, in 2014 and 2017, respectively.

From 2017 to 2019, he was a Postdoctoral Research Fellow with UWA. He is currently an Assistant Professor with Deakin University, Melbourne, VIC, Australia. His research interests include power system analysis, renewable energy integration and forecasting, and power electronics and its applications and control.

Dr. Yu received the First and Second Best Paper Awards in IEEE Australia Paper Competition, in 2016 and 2017, respectively, the Best Reviewer Award of the IEEE TRANSACTIONS ON SMART GRID, in 2018, and Featured Article in Chaos an Interdisciplinary Journal of Nonlinear Science, 2019.

Pinjia Zhang (Senior Member, IEEE) received the B.Eng. degree from Tsinghua University, Beijing, China, in 2006, and the master's and Ph.D. degrees from the Georgia Institute of Technology, Atlanta, GA, USA, in 2009 and 2010, respectively, all in electrical engineering.

From 2010 to 2015, he was with the Electrical Machines Laboratory, GE Global Research Center, Niskayuna, NY, USA. Since 2015, he has been with the Department of Electrical Engineering, Tsinghua University as an Associate Professor. He has authored and coauthored more than 80 papers in refereed journals and international conference proceedings, has more than 40 patent fillings in the U.S. and worldwide. His research interests include condition monitoring, diagnostics and prognostics techniques for electrical assets.

Dr. Zhang was the recipient of the IAS Andrew W. Smith Outstanding Young Member Achievement Award in 2018. He also received three Best Paper Awards from the IEEE IAS and IES Society.

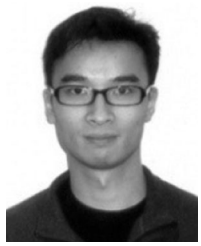

Herbert H. C. Iu (Senior Member, IEEE) received the B.Eng. (hons.) degree in electrical and electronic engineering from the University of Hong Kong, Hong Kong, in 1997, and the Ph.D. degree from the Hong Kong Polytechnic University, Hong Kong, in 2000.

In 2002, he joined as a Lecturer with the School of Electrical, Electronic and Computer Engineering, The University of Western Australia, Crawley, WA, Australia, where he is currently a Professor. He is a Co-Editor of *Control of Chaos in Nonlinear Circuits and Systems* (Singapore: World Scientific, 2009) and a co-author of *Development of Memristor Based Circuits* (Singapore: World Scientific, 2013). His research interests include power electronics, renewable energy, nonlinear dynamics, current sensing techniques, and memristive systems. He has authored and coauthored more than 100 papers in these areas.

Dr. Iu received two IET Premium Awards, in 2012 and 2014. In 2014, he also received the Vice-Chancellor's Mid-Career Research Award. He currently serves as an Associate Editor for the *International Journal of Bifurcation and Chaos* and IEEE Circuits and Systems Society Newsletters, and an Editorial Board Member for the *Australian Journal of Electrical and Electronics Engineering*.

Tyrone Fernando (Senior Member, IEEE) received the B.Eng. (hons.) and doctoral degrees in philosophy from the University of Melbourne, Parkville, VIC, Australia, in 1990 and 1996, respectively.

In 1996, he joined the School of Electrical Electronic and Computer Engineering (EECE), University of Western Australia, Crawley, WA, Australia, where he was the Deputy Head of the School from 2009 to 2010, and is currently a Professor. He has served as an Associate Editor for the IEEE TRANSACTIONS ON INFORMATION TECHNOLOGY IN BIOMEDICINE and also as a Guest Editor for the journal of *Optimal Control Applications and Methods*. He has authored many journal and conference articles and two books in the areas of functional observers and closed-loop control of blood glucose in diabetics. His research interests include estimations theory, control theory and application of control theory to smart grids, power systems, circuits and systems, and biomedical engineering.